Pacific Subtropical Cell Response to Reduced Equatorial Dissipation

M. J. HARRISON AND R. W. HALLBERG

NOAA/GFDL, Princeton, New Jersey

(Manuscript received 2 October 2006, in final form 15 January 2008)

ABSTRACT

Equatorial turbulent diffusivities resulting from breaking gravity waves may be more than a factor of 10 less than those in the midlatitudes. A coupled general circulation model with a layered isopycnal coordinate ocean is used to assess Pacific climate sensitivity to a latitudinally varying background diapycnal diffusivity with extremely low values near the equator.

The control experiments have a minimum upper-ocean diffusivity of 10^{-5} m^2 s^{-1} and are initialized from present-day conditions. The average depth of the $\sigma_\theta = 26.4$ interface ($z_{26.4}$) in the Pacific increases by ~140 m after 500 yr of coupled model integration. This corresponds to a warming trend in the upper ocean. Low equatorial diffusivities reduce the $z_{26.4}$ bias by ~30%. Isopycnal surfaces are elevated from the eastern boundary up to midlatitudes by cooling in the upper several hundred meters, partially compensated by freshening. Entrainment of intermediate water masses from below $\sigma_\theta = 26.4$ decreases by ~1.5 Sv (1 Sv $\equiv 10^6$ m^3 s^{-1}), mainly in the western tropical Pacific. The Pacific heat uptake (30°S–30°N) from the atmosphere reduces by ~0.1 PW. This is associated with warmer entrainment temperatures in the eastern equatorial Pacific upwelling region. Equatorward heat transport from the Southern Ocean increases by ~0.07 PW.

Reducing the upper-ocean background diffusivity uniformly to 10^{-6} m^2 s^{-1} cools the upper ocean from the tropics, but warms and freshens from the midlatitudes. Enhanced convergence into the Pacific of water lighter than $\sigma_\theta = 26.4$ compensates the reduction in upwelling of intermediate waters in the tropics. Basin-averaged $z_{26.4}$ bias increases in the low background case.

These results demonstrate basin-scale sensitivity to the observed suppression of equatorial background dissipation. This has clear implications for understanding oceanic heat uptake in the Pacific as well as other important aspects of the climate system. Diapycnal diffusivities due to truncation errors and other numerical artifacts in ocean models may need to be less than 10^{-6} m^2 s^{-1} in order to accurately represent this effect in climate models.

1. Introduction

Near-inertial wind and tidally generated waves dominate the internal gravity wave field (see, e.g., Alford 2003). Their propagation, interaction with the large-scale flow, and mutual interaction is unresolvable in climate models. Instead, they are subject to numerical dissipation, and their imprint on the mean state of the ocean is represented by homogeneous time-invariant diapycnal diffusivities of $O(10^{-5})$ m^2 s^{-1} in most climate model applications. Depth-dependent mixing is commonly used, with larger values above rough topography in weak stratification (Bryan and Lewis 1979; Simmons et al. 2004). Localized regions of strong tidal topographic interaction can generate "hot spots" for cross-isopycnal mixing (Endoh and Hibiya 2006). Sufficiently large background mixing has been shown to be related to dense water production in numerical models in subpolar regions (Bryan 1987; Samelson and Vallis 1997; Gnanadesikan et al. 2003). Its importance for the shallower tropical circulation has been discussed as well (Yu and Schopf 1997; Lu and McCreary 1995).

Gravity waves are excited by winds, tidal and nontidal flow interactions with topography (see, e.g., Legg and Huijts 2006), and along-frontal regions. Subsequent interactions, either within the wave field itself or with its environment, transport wave energy toward high vertical wavenumbers where turbulent dissipation occurs. A fraction of the decay of turbulent energy does work to raise the potential energy of the mean state of

Corresponding author address: M. J. Harrison, NOAA/GFDL, P.O. Box 308, Princeton, NJ 08542-0308.
E-mail: matthew.harrison@noaa.gov

DOI: 10.1175/2008JPO3708.1

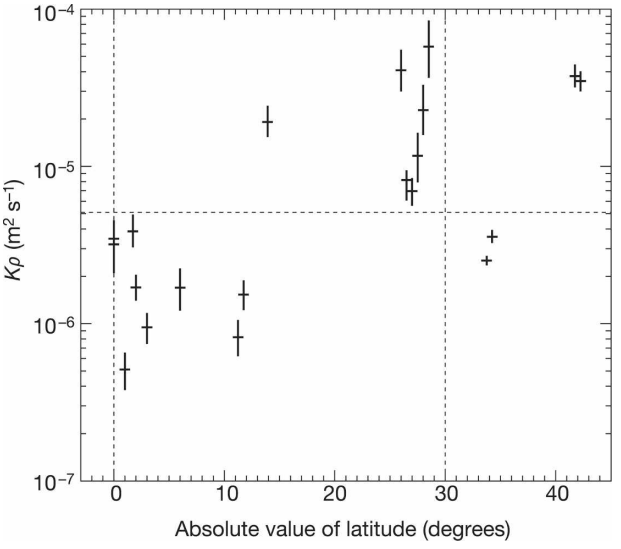

FIG. 1. Reproduced from Gregg et al. (2003, their Fig. 2). Diapycnal diffusivities calculated using observed dissipation rates and stratification from microstructure observations. The horizontal reference line is the diffusivity at 30° latitude when internal waves are at the level of the Garret and Munk (1991) spectrum. Owing to the latitude effect on dissipation produced by internal waves, intense internal waves observed near the equator produce only modest values of diffusivity.

the ocean via small-scale diapycnal overturns. Henyey et al. (1986, hereafter HWF) used Monte Carlo ray-tracing computations to derive an expression for the rate of dissipation resulting from wave–wave interactions as a function of the Coriolis parameter f and the ambient stratification. Their model predicts a dramatic reduction in the tropics. This is consistent with microstructure data. Assuming the thermal diffusivity is proportional to the inverse-squared buoyancy frequency N^{-2} times the turbulent dissipation, Gregg et al. (2003) calculated background diffusivities below the thermocline less than 10^{-6} m^2 s^{-1} near the equator, in comparison with subthermocline midlatitude values near 10^{-5} m^2 s^{-1}. Figure 1, reproduced from Gregg et al. (2003), shows microstructure estimates of background diapycnal diffusivities at various latitudes. The authors find a nearly tenfold decrease in diffusivities in the tropics, despite elevated internal wave activity in these regions, supporting the HWF theory. The link between a latitudinally varying dissipation model (a simplified version of HWF) and the subtropical–tropical circulation of the Pacific basin is the subject of this study.

The subtropical cell (STC; Luyten et al. 1983; McCreary and Lu 1994) encompasses the pathways whereby fluid parcels that subduct in midlatitudes are reconnected to the surface, from years to decades later, mainly in the eastern equatorial Pacific. Biological productivity in the eastern tropics is, for example, closely related to the transit time between these locations as well as the integrated effect of mixing (Sarmiento et al. 2003).

Figure 2 shows the distribution of depth and planetary potential vorticity ($Q = N^2 f g^{-1}$) from Argo measurements on the $\sigma_\theta = 25.1$ and 26.4 isopycnals. The 25.1 surface intersects the core of the Equatorial Undercurrent (EUC) and outcrops near 30° latitude in both hemispheres. The lower fringes of the EUC lie in the 26.0–26.5 potential density range, which is characteristic of wintertime mixed layers between 40° and 50° latitude (Tsuchiya 1981; Toggweiler et al. 1991; Suga et al. 1997). Ideal fluid pathways correspond to Q isopleths. Note the high values of potential vorticity, or strong stratification, along the west coast of the Americas. Ventilated thermocline theory illustrates the importance of the eastern boundary for the interior solution (Luyten et al. 1983; Pedlosky 1983; Samelson and Vallis 1997). The major currents of the Pacific are revealed by the broadscale Q distribution at 25.1.

High-Q (low salinity) water extends into the tropics from the northeastern boundary along the California Current. The ridge near 10°N, extending toward the western boundary, is driven by upwelling-favorable winds under the intertropical convergence zone (ITCZ). This separates the westward North Equatorial Current (NEC) to the north from the eastward North Equatorial Countercurrent (NECC). Equatorward Sverdrup flow, originating from the subduction boundary to the north and east, is directed westward around the ITCZ barrier (Johnson and McPhaden 1999). A portion of this flow enters the tropics via the Mindanao Current; the remainder is either recirculated northward along the western boundary or feeds the Indonesian Throughflow (ITF; Fine et al. 1994). North Pacific Subtropical Mode Water is found near the northwestern subduction boundary (Bingham 1992). In the Southern Hemisphere, low-Q (high salinity) water dominates most of the subtropics and can be traced to mode water formed in the southeast subtropical Pacific (Wong and Johnson 2003).

The lower interface at $\sigma_\theta = 26.4$ outcrops poleward of 30° latitude and is observed within 100 m of the surface along portions of the eastern boundary and the Costa Rica Dome. Mode waters (low Q) formed near the separation of the East Australia Current (Roemmich and Cornuelle 1992) and along the Kuroshio Extension (Talley et al. 1995; Suga et al. 1997) occupy the western and central basins, respectively. The tropical pycnostad is a region of low equatorial Q bounded by latitudes near 3° in the west and 8°–10° in the eastern part of the basin. This is a well-observed but poorly

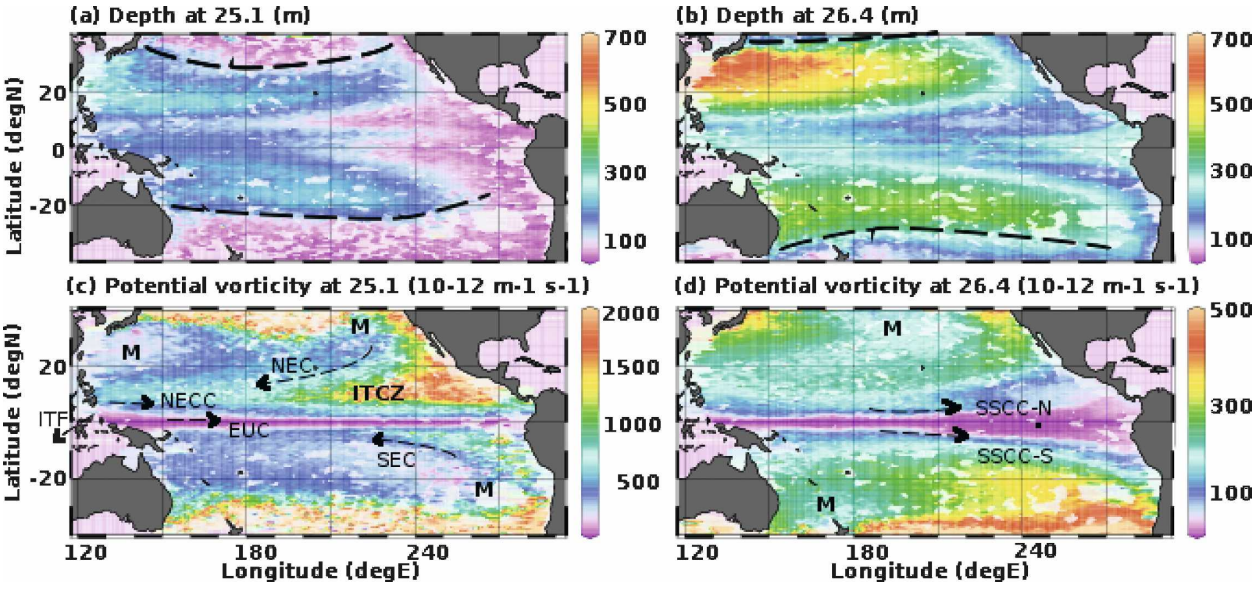

FIG. 2. (top) Isopycnal depths (m) and (bottom) potential vorticity (10^{-12} m^{-1} s^{-1}) sampled by the Argo network from 2000 to 2006 on potential density surfaces (left) 25.1 and (right) 26.4. The approximate subduction boundaries are indicated in (a) and (b). The major currents and mode water formation regions (M), as discussed in the text, are indicated in (c) and (d).

understood feature of the ocean (Jones 1973; Tsuchiya 1981). The front is associated with eastward subsurface countercurrents (SSCC-N and SSCC-S) with estimated transport in excess of 7 Sv (1 Sv $\equiv 10^6$ m^3 s^{-1}; Johnson and Moore 1997; Rowe et al. 2000). These jets may be connected to upwelling regions offshore of Peru and Central America (McCreary et al. 2002; Kessler 2002; Xie et al. 2005).

Consider the integrated layer continuity equation over a horizontal domain A, from the surface z_0 to $z_{26.4}$,

$$\partial_t \int_A \int_{z=z_0}^{z=z_{26.4}} dz\, dA + \int_S \int_{z=z_0}^{z=z_{26.4}} \mathbf{u}_i \cdot \hat{\mathbf{n}}\, dz\, dS = \int_A \partial_\rho(\kappa\rho_z)|_{z=z_{26.4}}\, dA + \int_A F|_{z_0}\, dA. \quad (1)$$

The first right-hand term is the volumetic entrainment rate at the $\sigma_\theta = 26.4$ interface, expressed as a Fickian diffusion. Apart from higher diffusivities resulting from interaction with the mixed layer or penetrating convection, κ is a function of the Richardson number and shear where it is less than a critical value; otherwise, it is equal to the background value. The second right-hand side term is the freshwater flux resulting from atmospheric sources, including precipitation and runoff. Here, $\mathbf{u}_i$ is the flow along surfaces of constant potential density and includes contributions from both resolved flow and eddy thickness flux parameterizations in numerical models (Gent and McWilliams 1990); $\mathbf{u}_i$ is integrated along the control volume boundary S, for example, lines of constant latitude, and $\hat{\mathbf{n}}$ is the unit inward vector normal to the boundary. In the Pacific, transport convergence from the subtropics above $\sigma_\theta = 26.4$ is balanced by turbulent entrainment from below, transport into the Indian Ocean (via the ITF) above $\sigma_\theta = 26.4$, and the time tendency of basin-averaged $z_{26.4}$ (surface freshwater contributions are relatively small). Most coupled climate models appear to suffer from excessive vertical drift in the upper pycnocline, the so-called diffuse thermocline problem. In this study, we address the following question: Are low equatorial diffusivities predicted by HWF and absent from climate models relevant to this common deficiency in climate simulations?

We present results using an isopycnal ocean model in stand-alone mode and coupled with the atmosphere–land–ice components of the National Oceanic and Atmospheric Administration (NOAA)/Geophysical Fluid Dynamics Laboratory (GFDL) Climate Model (CM2.1; Delworth et al. 2006) used in the Intergovernmental Panel on Climate Change (IPCC) Fourth Assessment Report (AR4). In uncoupled mode, the ocean surface fluxes are calculated using adjusted National Centers for Environmental Prediction (NCEP) reanalysis data and Quick Scatterometer (QuikSCAT) winds (Milliff et al. 2004). This model configuration is constrained to observations, allowing for a more direct comparison to data. The uncoupled model, however, lacks important atmospheric feedbacks, replacing them with overly strong negative thermal feedbacks. The fully coupled

configuration is more physically motivated. Changes in the atmospheric circulation and cloudiness, for instance, are represented in the model in an energetically consistent fashion.

The ocean model solves the Boussinesq primitive equations in isopycnal coordinates (Hallberg 2000; Hallberg and Gnanadesikan 2006). This allows for strict control of diapycnal diffusion in contrast to traditional z-coordinate models, which are subject to advection truncation errors (Griffies et al. 2000). The isopycnal model allows us to approach the adiabatic limit without difficulty. Sensitivity of the subtropical circulation has been documented in coupled and uncoupled general circulation models to levels near 25 times molecular thermal diffusivities or 10^{-5} m^2 s^{-1} (Yu and Schopf 1997; Meehl et al. 2001; Vallis 2000). Meehl et al. (2001) concluded, based on a suite of experiments with varying horizontal and vertical diffusivities, that lower values of background vertical diffusivity tend to produce a sharper thermocline and stronger ENSO variability. Canuto et al. (2004) tested the HWF parameterization with minimum tropical diffusivities as low as 10^{-6} m^2 s^{-1} using a z-coordinate model with fixed surface forcing. Likewise, they were able to construct a sharper equatorial thermocline. In this study, we present a broader context for understanding the relationship between mixing resulting from gravity wave dissipation and the Pacific circulation.

Section 2 contains a description of the model in uncoupled (UnCpld) and fully coupled (Cpld) configurations. Section 3 presents results from multicentury control integrations (CTRL) with mixing coefficients as a function of depth only. Section 4 documents the model response to low equatorial diffusivity (HWF) as well as a uniformly low value of 10^{-6} m^2 s^{-1} (LOW). Section 5 contains a summary of our findings followed by a brief discussion. Surface mixed layer densification during late wintertime conditions in midlatitudes is systematically underestimated in this model. This appears to be a significant contributor to model bias within the STC and will be addressed in future studies. Despite this shortcoming, these experiments provide evidence that the suppression of equatorial diffusivities resulting from breaking gravity waves can significantly impact the climate of the Pacific Ocean.

2. Model description

a. Ocean model

The ocean model is similar to that used in Hallberg and Gnanadesikan (2006). The model uses in situ density from the full equation of state for seawater for all dynamics (Wright 1997). Resolved shear-driven diapycnal mixing in the interior is based on the gradient Richardson number Ri as well as the width of the region of low Ri (Hallberg 2000). The critical Ri for elevated mixing has a value of 0.2 near the equator and 0.8 elsewhere, and the nondimensional shear mixing rate is 0.001 at the equator and increases to 0.1 within 10° latitude. This ad hoc parameterization produces a fairly realistic EUC as well as a sustained North Atlantic overturning circulation in this model. [A subsequent parameterization developed by Jackson et al. (2008) avoids the need for any such spatial dependence of its "constants."] The model also incorporates a two-layer Kraus–Turner-like bulk mixed layer and a two-layer variable density buffering region between the mixed layer base and the interior (Hallberg 2003). This buffering scheme allows high-frequency fluxes out of the mixed layer, on time scales less than several days, to be available for reentrainment into the surface mixed layer prior to mixing with the interior. The response to diurnal forcing is more realistic with the buffer layers included. Shortwave attenuation rates are determined from monthly varying satellite-derived chlorophyll estimates using the scheme described in Anderson et al. (2007). The ocean is global in extent, covering the Arctic with the tripolar grid configuration of Murray (1996).

There are 45 interior layers in potential density coordinates referenced to 2000 db. The horizontal resolution in the tropics is 1° zonally and ⅓° meridionally from 10°S to 10°N. The meridional resolution decreases toward 1° in the midlatitudes. The model includes a uniform lateral thickness diffusion coefficient of 900 m^2 s^{-1} and a lateral Laplacian viscosity, which scales as the grid spacing times a velocity scale of 0.01 m s^{-1} (e.g., 10^3 m^2 s^{-1} for a 100-km grid box). The reference background diapycnal diffusivity is horizontally uniform and increases with depth to simulate topographic effects (Bryan and Lewis 1979). The diffusivity transitions from its surface value of 10^{-5} m^2 s^{-1} to a deep-ocean value of 10^{-4} m^2 s^{-1} between 1000 and 2500 m. The ratio of background diapycnal diffusivity to viscosity is 0.1 for these experiments.

Three ocean configurations are chosen: a constant background surface diapycnal diffusivity $\kappa_0 = 10^{-5}$ m^2 s^{-1} (CTRL), a latitudinally varying upper-ocean diffusivity (HWF), and a uniformly lower background surface diffusivity of 10^{-6} m^2 s^{-1} (LOW). In HWF, the surface background diffusivity is

$$\kappa_s(\phi) = \max[10^{-7}, \kappa_0 |f/f_{30}| \cosh^{-1}(1/f)/\cosh^{-1}(1/f_{30})], \quad (2)$$

where f_{30° is the Coriolis frequency at 30° latitude. The two-dimensional equation for the diffusivity is

$$\kappa(\phi, z) = \kappa_s(\phi) + \Gamma \text{atan}\left(\frac{H_t}{\delta_t}\right) + \Gamma \text{atan}\left[\frac{z - \mathrm{H}_t}{\delta_t}\right],$$

$$\Gamma = (\kappa_d - \kappa_s)/\left[0.5\pi + \text{atan}\left(\frac{H_t}{\delta_t}\right)\right], \quad (3)$$

where H_t = 2500 m, δ_t = 222 m, and κ_d is the deep-ocean diffusivity of 10^{-4} m^2 s^{-1}. Diffusivities at depth are identical in the CTRL, HWF, and LOW experiments. In these experiments, the deep-ocean diffusivities are assumed to be controlled by separate processes, such as tidal interactions with topography, and therefore are not influenced by internal wave dynamics leading to the HWF latitudinal profile.

All experiments are initialized from rest using observed January mean interface depths, temperature, and salinity (*World Ocean Atlas 2001,* hereafter *WOA01*; Conkright et al. 2001).

b. Data atmosphere

In the UnCpld experiments, daily average 10-m atmospheric temperature and specific humidity, surface downwelling shortwave and longwave radiation, and precipitation from the NCEP reanalysis and QuikSCAT microwave scatterometer–derived 10-m winds (Milliff et al. 2004) from 2000 to 2004 are used as inputs to bulk formula calculations. A climatological correction is applied to the downwelling radiation and precipitation using satellite-derived fluxes. River runoff is not included. A restoring of surface salinity to *WOA01* monthly climatological 5-m values is applied at a freshwater flux rate of approximately 5 mm day^{-1} per unit psu difference. A sea ice model (Winton 2000) predicts sea ice extent and thickness. Bulk formula surface flux calculations and adjustments to the NCEP model output follow Large and Yeager (2004).

c. Coupled model

The isopycnal ocean model is coupled to the atmosphere–land–ice components described in Delworth et al. (2006). A comprehensive description of the tropical Pacific in a version of the model coupled with a z-coordinate ocean model, the fourth Modular Ocean Model (MOM4; Griffies et al. 2005), is described in Wittenberg et al. (2006). The atmospheric radiative flux is updated every 3 h with the inclusion of diurnal solar forcing and is based on 1990 climatological radiative gas concentrations. Atmospheric variables are computed on an approximate 2° latitude × 2.5° longitude grid spacing with 24 vertical levels. The atmospheric model uses a K-profile planetary boundary layer scheme (Lock et al. 2000), relaxed Arakawa–Schubert convection (Moorthi and Suarez 1992), and a prognostic cloud scheme (GFDL Atmospheric Model Development Team 2004). Atmospheric deep convection incorporates a simple parameterization for momentum transport that has been shown to impact the model's seasonal cycle amplitude and interannual variability in the tropical Pacific (Wittenberg et al. 2006).

3. Control experiments

We begin our presentation of the UnCpld-CTRL and Cpld-CTRL experiments by comparing annual mean surface heat, freshwater and momentum flux, maximum wintertime mixed layer density, Ekman pumping velocity, and gyre transport (Figs. 3–6). In both the UnCpld-CTRL and Cpld-CTRL experiments, peak mixed layer densities are underestimated compared to *WOA01* data near the subtropical–subpolar transition zone in both hemispheres (about 40°–50° latitude). This is significant because late-wintertime mixed layer properties help determine the temperature, salinity, Q, and other biogeochemical properties of the subducted fluid, which subsequently becomes part of the STC circulation. Consistent with the underestimate of wintertime mixed layer density in midlatitudes, the models exhibit a positive monotonic trend in basin-averaged $z_{26.4}$. Initial model drift in midlatitudes occurs at the northwest and southwest corners of the basin near the Kuroshio–Oyashio merger and East Australia Current separation (Figs. 8 and 9). Tropical biases emerge from the eastern tropics and along the eastern boundary. Direct comparisons are made between the UnCpld-CTRL model and the 140°W, equator Tropical Atmosphere Ocean (TAO/TRITON) mooring (Hayes et al. 1991; Fig. 7). This provides some validation of the quality of the model simulation. We note the absence of additional sources of mixing, beyond that provided by the background parameterization, below the core of the EUC. This is inconsistent with observations of elevated turbulence in this region (Peters et al. 1995).

a. UnCpld-CTRL

1) Annual mean surface fluxes and wintertime mixed layer density

The UnCpld experiments are integrated using repeat cycles of 2000–04 forcing data for 150 yr. We chose this

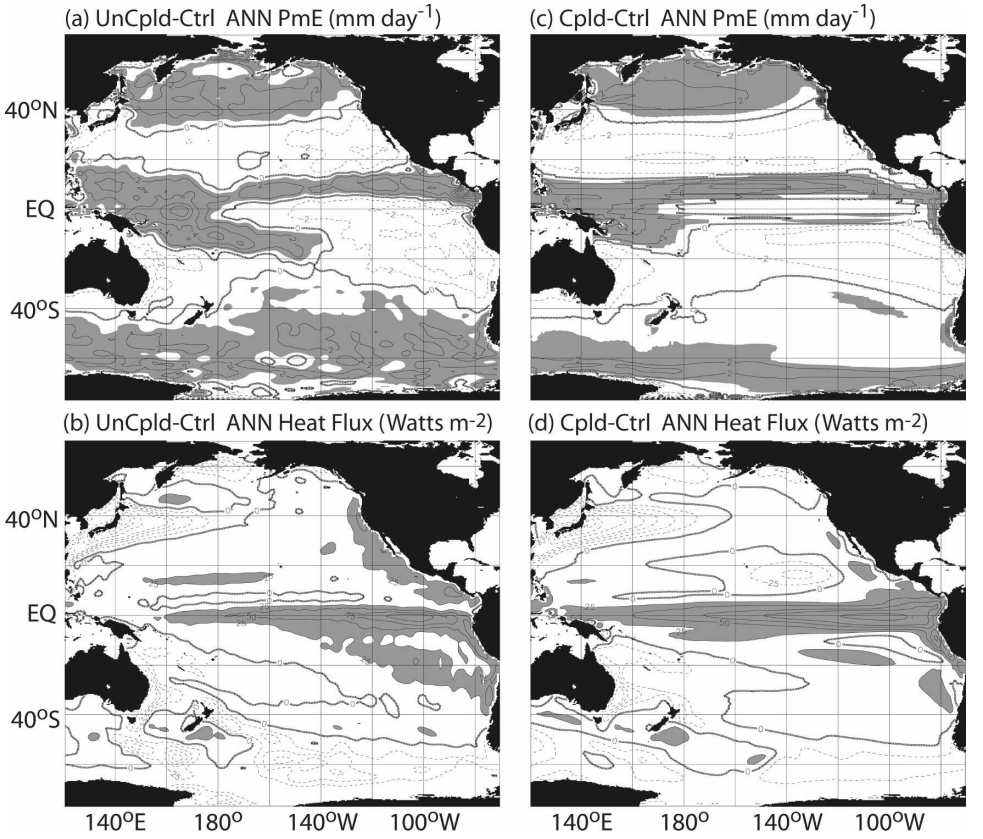

FIG. 3. Annual mean (top) net precipitation (contour interval = 2 mm day^{-1}) and (bottom) heat flux (contour interval = 25 W m^{-2}, 50 W m^{-2} above 100), for the (left) UnCpld-CTRL and (right) Cpld-CTRL experiments averaged between model years 51–60 and 301–400, respectively. Precipitation greater than 2 mm day^{-1} and heat flux greater than 25 W m^{-2} are shaded.

period because of the availability of high-quality QuikSCAT winds and TAO/TRITON data. In early 2000, a moderate La Niña event peaked in the eastern tropics and in 2003 a weak El Niño took place. Results are averages from model years 51–60, unless otherwise noted.

Figure 3 shows annual mean freshwater and heat flux. Within the ITCZ, net precipitation minus evaporation (PmE) exceeds 5 mm day^{-1}. The SPCZ extends diagonally from its northwestern extension, where it merges with the northern ITCZ, toward 20°S, 140°W. The dry eastern subtropical highs are centered near 35°N, 140°W and 30°S, 90°W. In the midlatitude storm-track regions, precipitation exceeds evaporation. Maximum cooling near the Kuroshio western boundary separation is in excess of 300 W m^{-2}. Peak warming in the Niño-3 region (5°S–5°N, 150°–90°W) is approximately 120 W m^{-2}. Basin-averaged heat and freshwater input from the atmosphere is 1.5×10^{15} W (1.5 PW) and -0.03 Sv, respectively.

Positive sea surface temperature (SST) biases exceeding 2°C occur in the eastern tropics, along the Peruvian and California coastal boundaries and in the subpolar regions in both hemispheres (not shown). Equatorward of 40° latitude, average (monthly RMS) SST differences compared to the *WOA01* climatology are +0.4°C (2.4°C). Surface salinity (SSS) has a more uniform fresh bias with an average (RMS) difference of −0.3 (0.3) PSU.

Figures 4a and 4b show the peak wintertime surface density (based on a monthly climatology) for the UnCpld-CTRL run and the *WOA01* analysis. It is clear from the figure that water mass production is biased toward lighter densities over most of the domain. For instance, $\sigma_\theta = 25.1$ water observed in the southeast Pacific offshore of Peru (between 5° and 20°S to the east of 100°W) is located more than 1000 km to the south offshore of southern Chile. The same is true for the northeast Pacific. Wintertime surface densities greater than $\sigma_\theta = 26.4$ are observed near the surface in the northwest Pacific poleward of 40°N, but are almost entirely absent in the model simulation.

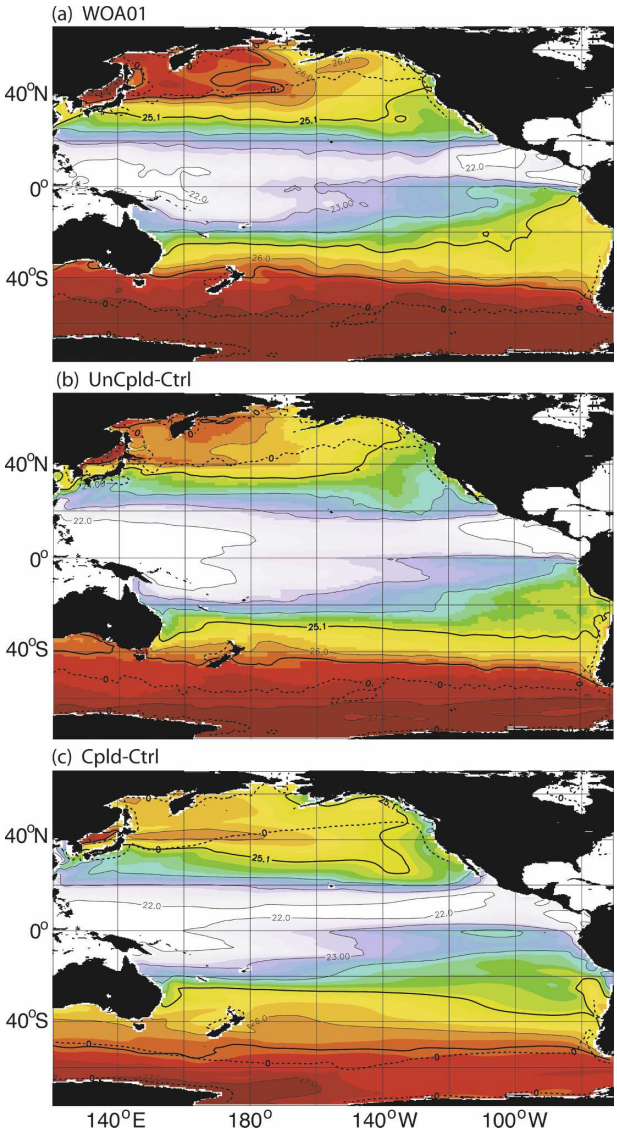

FIG. 4. Peak wintertime monthly averaged surface densities from the (top) *WOA01*, (middle) UnCpld-CTRL, and (bottom) Cpld-CTRL. Contour interval = 1 g kg^{-1}. The σ_θ = 25.1 and 26.4 isopycnal contours are highlighted (thick solid) along with the zero wind stress curl climatology (dashed) from (top and middle) the UnCpld-CTRL and (bottom) the Cpld-CTRL experiments.

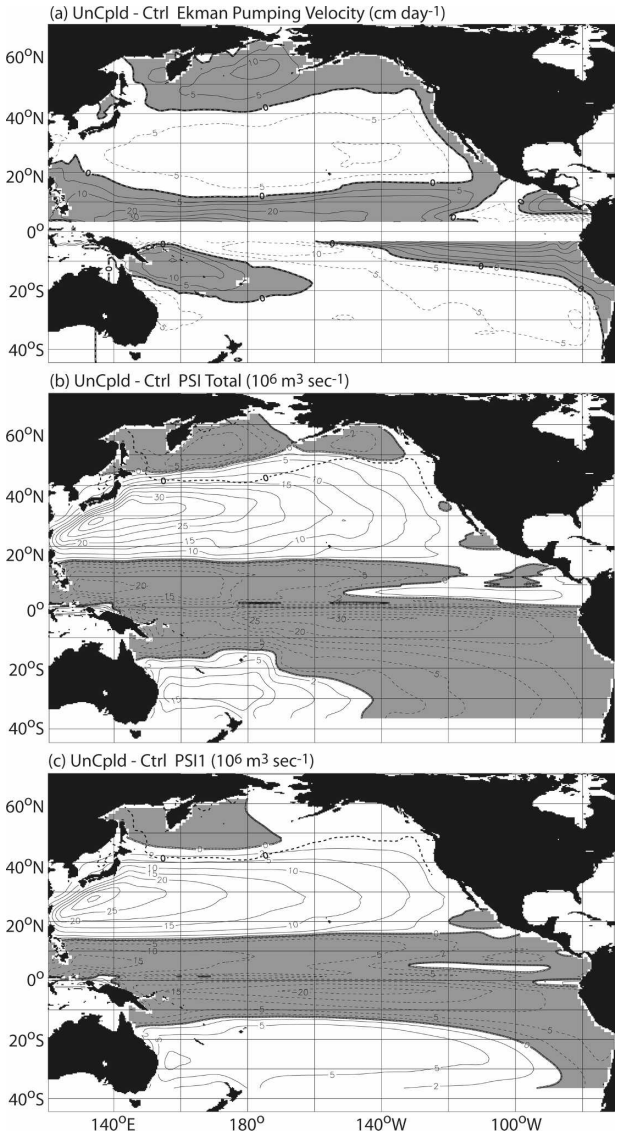

FIG. 5. (a) UnCpld-CTRL annual mean Ekman pumping velocity, (b) depth-integrated transport streamfunction, and (c) UL streamfunction. Positive (upward) Ekman velocity is shaded with a contour interval of 10 cm day^{-1} plus the ±5 cm day^{-1} contours. Cyclonic gyres are shaded with a contour interval of 5 Sv. The zero wind stress curl line near the subtropical/subpolar gyre boundary is indicated by the thick dashed lines.

2) OCEAN TRANSPORT

Annual mean Ekman pumping velocity is shown in Fig. 5 along with the depth-integrated transport streamfunction and the transport integrated to the σ_θ = 26.4 density interface [hereafter the upper layer (UL)]. Cyclonic gyres are shaded. Total western boundary transports exceed 40 Sv (35 Sv in the UL) along the Kuroshio, 20 Sv (15 Sv in the UL) for the Mindanao, 15 Sv (10 Sv in the UL) along the New Guinea Boundary Current, and 15 Sv (10 Sv in the UL) for the East Australia Current. The flow of water from southern latitudes is connected to equatorial upwelling with entry points along the New Guinea current and in the interior. Circulation from the Northern Hemisphere enters the tropics mostly from the western boundary.

Depth-integrated transport into the Pacific basin from the Southern Ocean is tied to ITF transport and the smaller exchange with the Arctic through the Bering Strait. The total oceanic transport convergence into

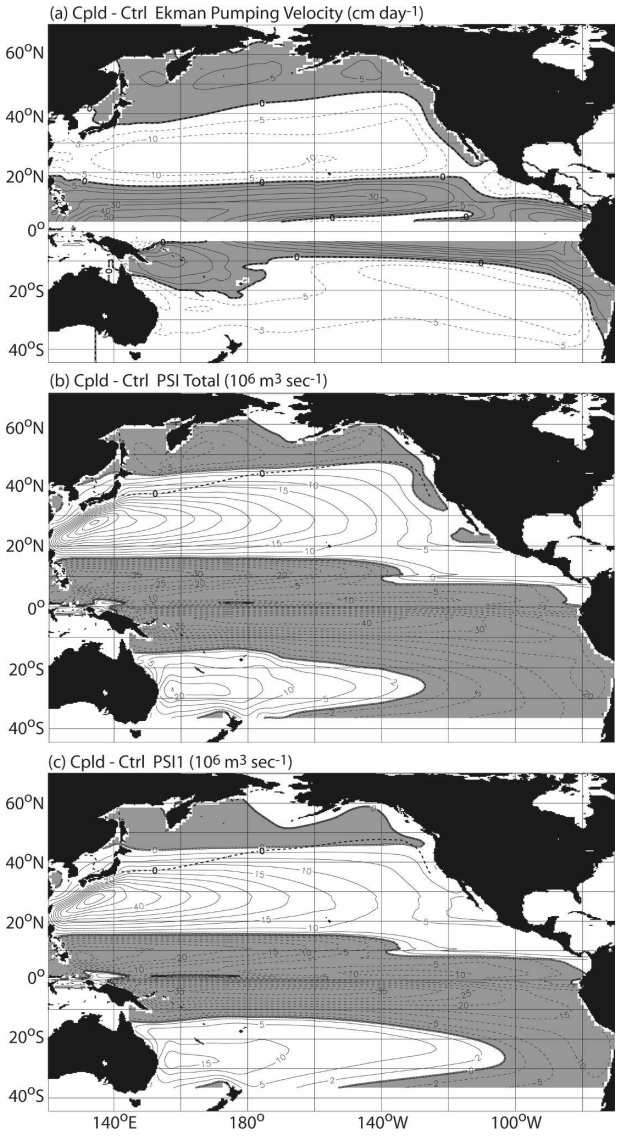

FIG. 6. As in Fig. 5, but for Ekman pumping and depth and transports for the Cpld-CTRL experiment.

the Pacific basin equatorward of 30° latitude balances the −0.03-Sv freshwater forcing from the atmosphere. Partitioning the transport by density class quantifies the overturning circulation. Toward the end of the 150-yr integration, net ocean transport into the Pacific across 30°S is ~13 (6 in the UL) Sv. (Positive values are into the Pacific basin.) ITF transport to the Indian Ocean is approximately −12 (−10 in the UL) Sv. At 30°N, depth-integrated flow is fairly steady at −0.5 Sv (−1 Sv in the UL). Net Pacific export at densities less than σ_θ = 26.4 decreases monotonically from approximately −10 to −5 Sv over the 150-yr run. Entrainment of densities greater than σ_θ = 26.4 decreases from ~11 to 8 Sv. Correspondingly, basin-averaged $z_{26.4}$ is increasing at a rate of 1–3 Sv. In other words, "light" water is accumulating in the Pacific.

3) PYCNOCLINE DRIFT

Figure 8 illustrates the drift in the depth of the σ_θ = 26.4 isopycnal surface to year 150 of the UnCpld-CTRL experiment. Basin-averaged $z_{26.4}$ is increasing at an average rate of ~0.6–0.8 m yr^{-1}. This corresponds to a warming and freshening trend in the upper several hundred meters. The model adjustment to the forcing involves an initial deepening of the σ_θ = 26.4 surface in the eastern equatorial Pacific and along the midlatitude subduction boundaries. Erosion of the tropical pycnostad is initiated by deepening on the flanks of the low-Q region in the eastern equatorial Pacific. Along the eastern boundary, $z_{26.4}$ increases by more than 150 m. Too-light wintertime mixed layers in midlatitude subduction regions result in an upward shift in the distribution of mode and intermediate waters in both hemispheres. This pushes the σ_θ = 26.4 surface to deeper levels. Equatorward propagation is suggested by the figure. Positive $z_{26.4}$ anomalies originate in the northwest and southwest Pacific and can be traced eastward and equatorward in the figure.

4) COMPARISON TO TAO TRIANGLE TRANS-OCEAN BUOY NETWORK MOORING AT 0°, 140°W

Daily UnCpld-CTRL zonal current and temperature are shown in Fig. 7 at 0°, 140°W. Comparisons are made to 5-m-resolution acoustic current meter and 5–15-m-resolution thermistor measurements from the TAO/TRITON mooring array. Model and data are linearly interpolated to a common grid of daily resolution and 10-m vertical spacing. Overall, the variability from the model is quite reasonable. The 2000 La Niña and 2003 El Niño are simulated fairly well in the model at the mooring location. The seasonal migration of the EUC compares favorably to ADCP measurements. A noticeable inconsistency is the weak vertical shear above and below the EUC core. The gradient Richardson number Ri is suppressed in the region immediately below the undercurrent due to moderate shear, but not sufficiently to generate turbulence, which occurs for values of Ri less than about 0.2 in this experiment. Observations suggest that intermittent turbulence exists below the undercurrent (Peters et al. 1995).

Model-diagnosed shear production below the EUC core is negligible, and there are no additional parameterizations of mixing beyond the uniform background value of 10^{-5} m^2 s^{-1}. To the extent that in reality ad-

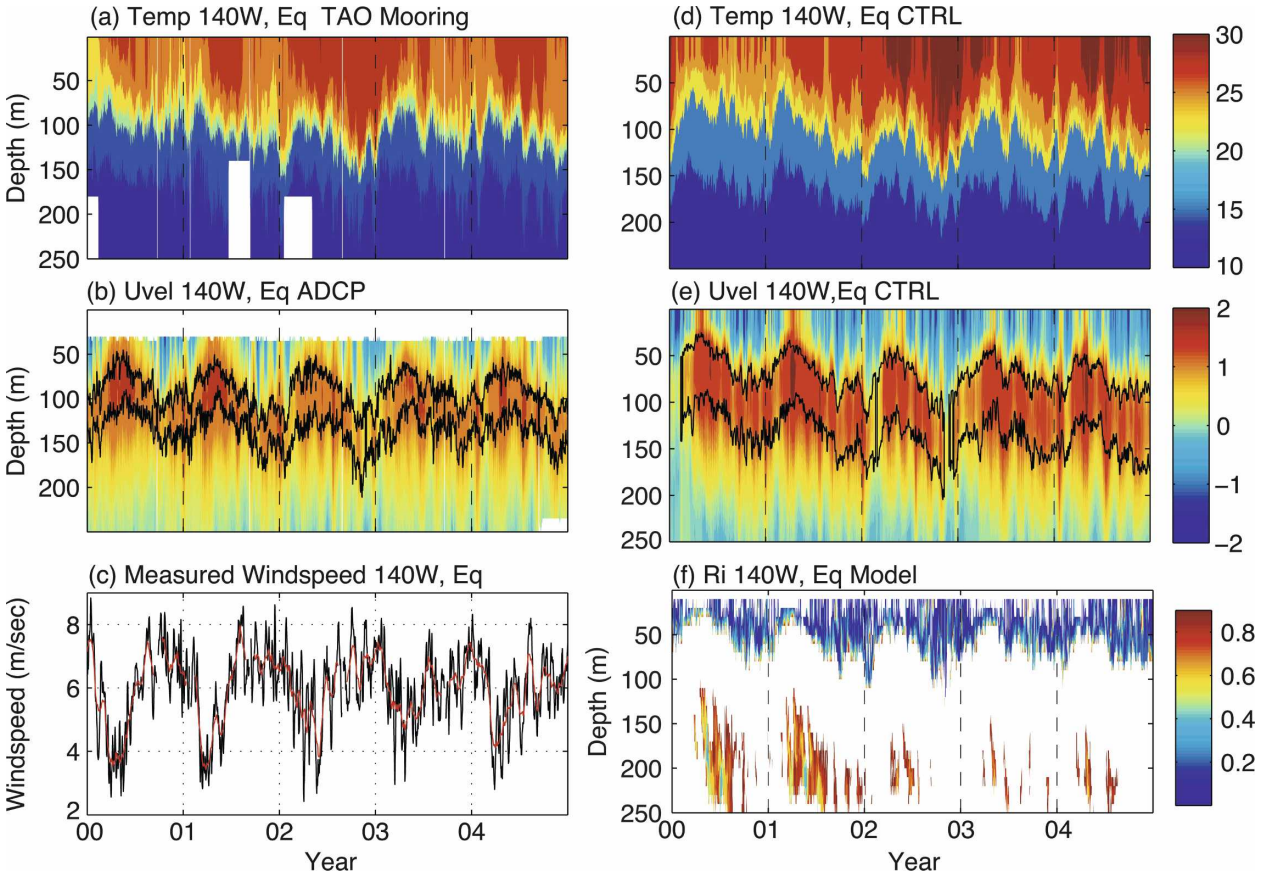

FIG. 7. Daily average (left) TAO/TRITON mooring data and (right) UnCpld-CTRL time series at 0°, 140°W. (top) Temperature (°C); (middle) zonal velocity (m s^{-1}), contours show the approximate width of the EUC core where the velocity is 0.2 m s^{-1} less than the EUC core defined as the maximum eastward velocity greater than 0.5 m s^{-1}; (bottom left) TAO anemometer wind speed (m s^{-1}) smoothed with a 5- (black) and 30-day (red) boxcar filter; (bottom right) gradient Richardson number Ri, resulting from resolved model stability and shear. Values less than 0.2 result in elevated diapycnal mixing in the present model. Values greater than 1.0 are not contoured.

ditional sources of mixing exist near the base of the EUC and elsewhere in the tropics, our results should be interpreted as providing an upper bound on the sensitivity to the background parameterization.

b. *Cpld-CTRL*

1) ANNUAL MEAN SURFACE FLUXES AND WINTERTIME MIXED LAYER DENSITY

The fully coupled model is integrated for 500 yr. Net precipitation in the ITCZ is generally higher than the UnCpld-CTRL run (Fig. 3), with a discernible band south of the equator, typical of most global climate models (Dai 2006). Noticeable differences in surface heat flux are found along the equator. Peak heat fluxes are in excess of 175 W m^{-2} in the Niño-3 region (120 W m^{-2} in UnCpld-CTRL). Peak zonal mean freshwater flux in the tropical Pacific is 7.8 mm day^{-1} (4.7 mm day^{-1} in UnCpld-CTRL). Net evaporation within the dry subtropical highs is correspondingly higher. Basin-integrated atmospheric heat and freshwater input (including land runoff) is 1.6 PW and −0.25 Sv, respectively (1.5 PW and −0.03 Sv in UnCpld-CTRL).

Peak annual mean SST biases compared to *WOA01* data are greater than 3°C along the eastern tropical and subtropical boundary and in the Southern Ocean [average (monthly RMS) error is +0.2°C (2.0°C) from 40°S to 40°N]. Near-surface salinity has a positive bias in excess of 1 PSU in the far eastern equatorial Pacific and portions of the eastern boundary offshore of 30°S and 25°N. The average (RMS) difference compared to *WOA01* data is −0.3 (0.5) PSU. High-latitude fresh biases exceed 1 PSU in subpolar regions. Wintertime mixed layer biases are qualitatively similar to the UnCpld-CTRL experiment (Fig. 4c). Peak mixed layer density in the northwest Pacific, southeast Pacific, and

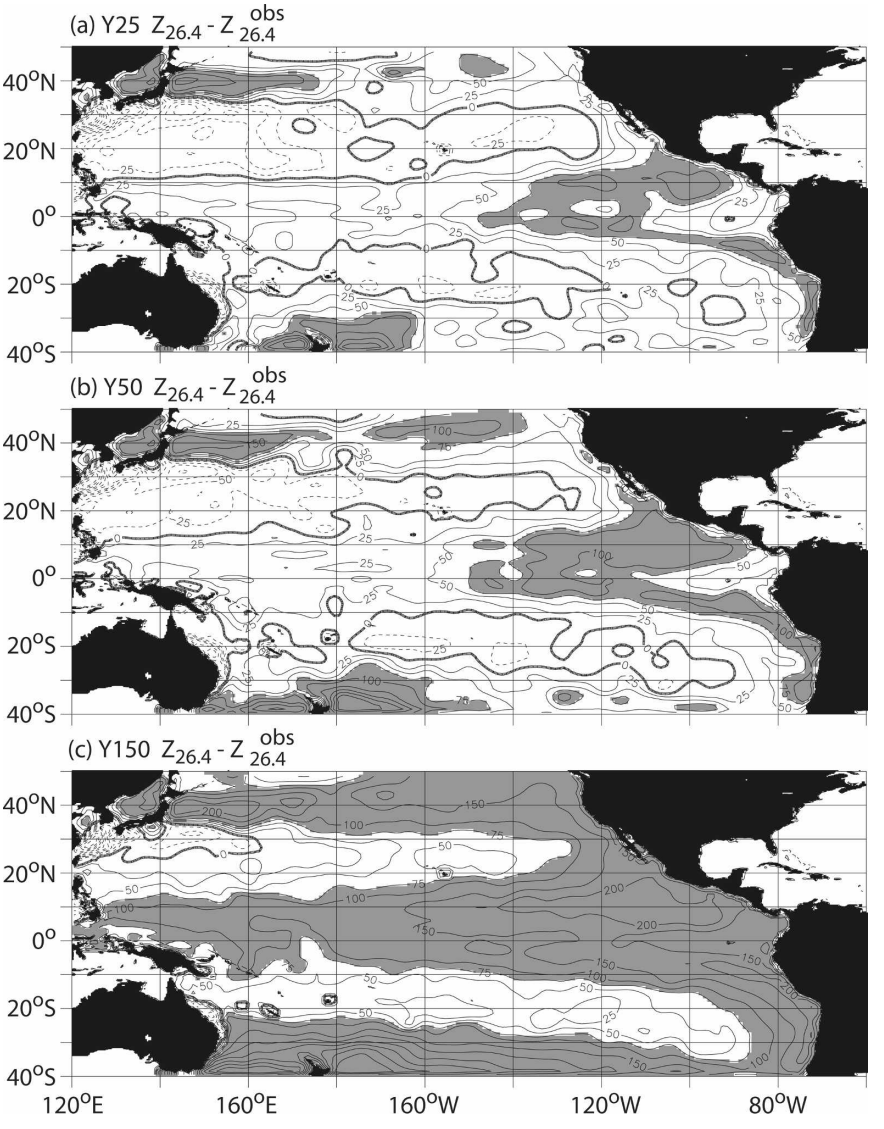

FIG. 8. UnCpld-CTRL $z_{26.4}$ difference from the *WOA01* climatology at years 25, 50, and 150 (contour interval = 10 m). Positive bias exceeding 75 m are shaded.

Southern Ocean are systematically underestimated in the model.

2) OCEAN TRANSPORT

Annual mean Ekman pumping velocity and gyre transports are shown in Fig. 6. Equatorial and subtropical gyre transports are higher than UnCpld-CTRL. The increase in gyre transport is consistent with the increase in the strength of the atmospheric circulation and stronger Ekman pumping in the Cpld model. Total western boundary current transports exceed 65 Sv (55 Sv in the UL) along the Kuroshio, 35 Sv (30 Sv in the UL) in the Mindanao, 30 Sv (30 Sv in the UL) for the New Guinea Current, and 20 Sv (15 Sv in the UL) for the East Australia Current. Total equatorward transport across 30°S is ~17 (9 in the UL) Sv near the end of the integration. ITF transport is approximately −16 (−12 in the UL) Sv, about −1 (−2 Sv in the UL) Sv past 30°N. The rate of entrainment from below $\sigma_\theta = 26.4$ within 30° latitude is fairly steady at ~6 Sv over the last 200 yr of the run. The bulk of the entrainment of intermediate water masses in the model occurs in the western tropical Pacific. Net along-isopycnal flow out of the Pacific basin above $\sigma_\theta = 26.4$ is about 5 Sv over the last 200 yr of the run. Upper-layer water is accumulating at a rate of ~1 Sv between years 300 and 500 associated with an upper-ocean warming trend.

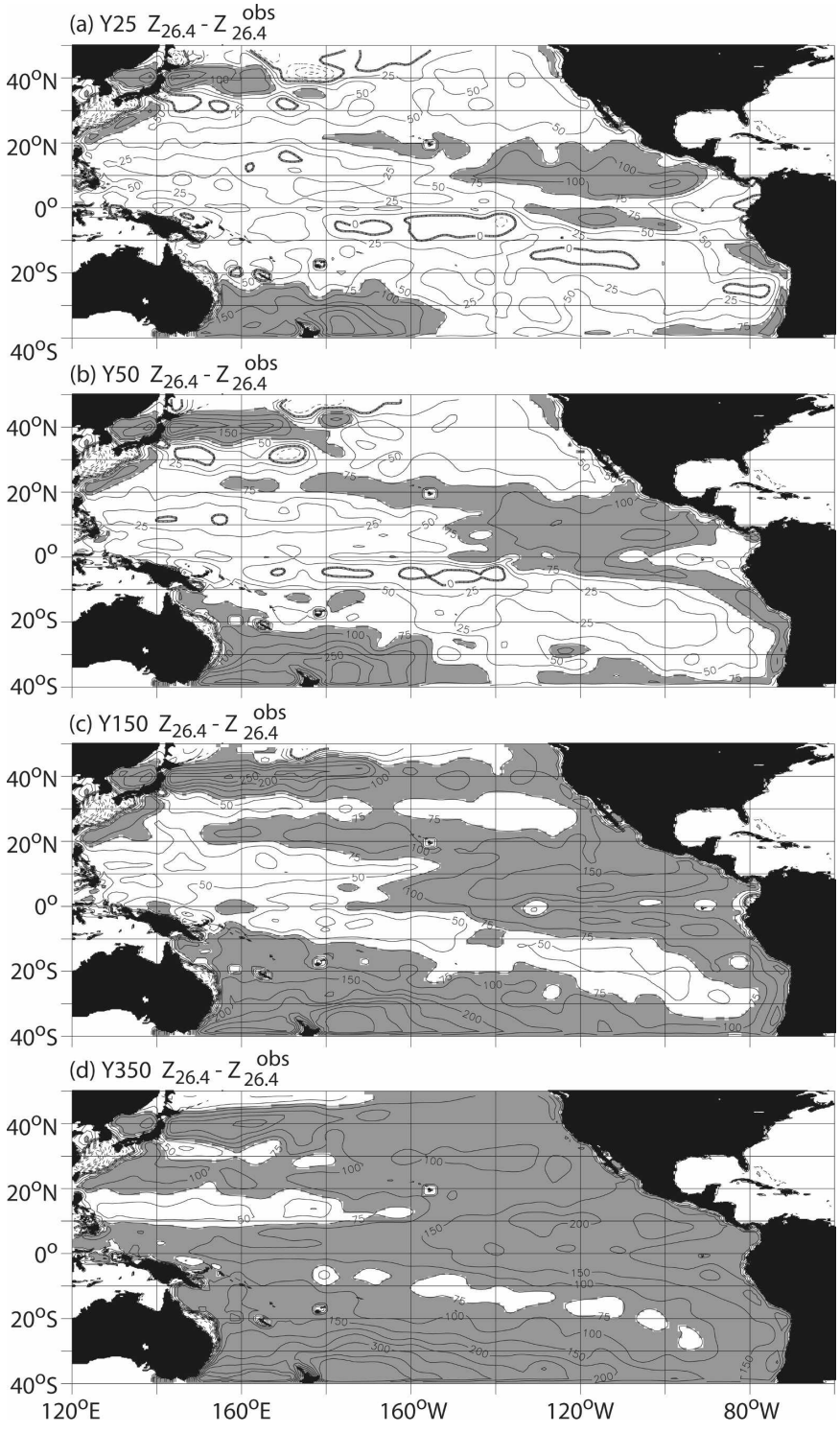

FIG. 9. Cpld-CTRL $z_{26.4}$ difference from the *WOA01* climatology at years 25, 50, 150, and 350 (contour interval = 25 m). Positive bias exceeding 75 m are shaded.

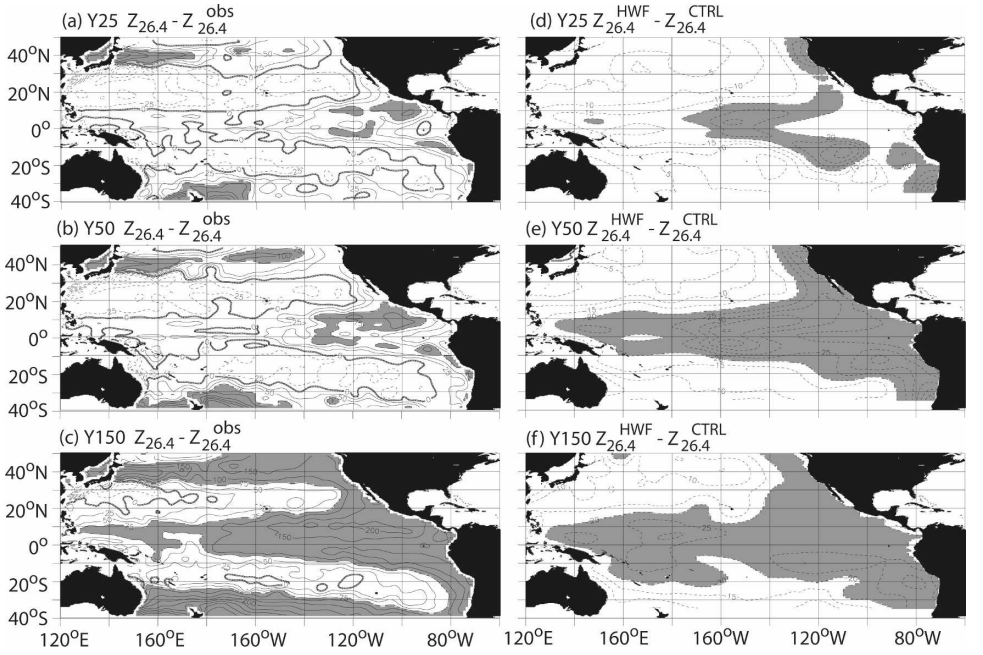

FIG. 10. (left) UnCpld-HWF minus *WOA01* $z_{26.4}$ (contour interval = 25 m). Positive biases exceeding 75 m are shaded. (right) UnCpld-HWF minus UnCpld-CTRL $z_{26.4}$ (contour interval = 5 m). Negative values larger than 20 m are shaded.

3) PYCNOCLINE DRIFT

Figure 9 is similar to Fig. 8. The deepening of the $\sigma_\theta = 26.4$ interface from the pycnostad region in the eastern tropics, the boundaries in the northwest and southwest Pacific, and near the eastern boundaries is reproduced in both the UnCpld-CTRL and Cpld-CTRL runs. The interface drifts in excess of 150 m over the course of the run across much of the Pacific. Along the eastern boundary, the upper-layer interface is more than 100 m deeper than observed by year 150. Drifts emerge from the subduction regions in the northwest and southwest Pacific. The deepening of $z_{26.4}$ in the model is largely associated with upper-ocean warming in the tropics and subtropics and freshening within the subpolar regions (not shown).

4. Model sensitivity

The UnCpld-HWF and Cpld-HWF experiments are identical to the CTRL runs, with the exception of the background gravity wave mixing parameterization described by Eq. (2). The models were integrated for 150 and 400 yr, respectively. The UnCpld-HWF and Cpld-HWF experiments exhibit a similar sensitivity pattern, but the response in Cpld-HWF is larger. Enhanced stratification and upper-ocean cooling is efficiently redistributed from the equator to the midlatitude eastern boundaries by Kelvin and coastally trapped waves.

For the Cpld experiments, we calculate the volumetric budget of water lighter than $\sigma_\theta = 26.4$ using Eq. (1). Reduced entrainment of intermediate waters in the western tropics compensates the positive trend in $z_{26.4}$ and cools the upper ocean. It is perhaps counterintuitive that reducing the entrainment of colder, denser water from below the thermocline should result in a cooling trend. Indeed, in the absence of thermal coupling at the air–sea interface, the expected response would entail warming above the thermocline and cooling below. Coupling to the atmosphere facilitates the release of oceanic heat by exposing warmer temperatures from below the mixed layer to the surface in the eastern equatorial upwelling region. In the Cpld experiment, equatorward transport of heat from the Southern Ocean compensates ~80% of the decrease in atmospheric heat uptake based on a 400-yr experiment.

a. UnCpld-HWF

Figure 10 shows UnCpld-HWF minus UnCpld-CTRL $z_{26.4}$ through year 150. By year 25, $z_{26.4}$ is reduced by as much as 40 m offshore of Oregon and Chile. Through year 50, average differences in the tropics are more than 20 m. The adjustment is maintained through 150 yr, although there is some indication that the solutions are converging. Annual mean Niño-3 temperatures are ~0.5°C warmer and salinity is more than 0.1 PSU higher. Offshore of North and South

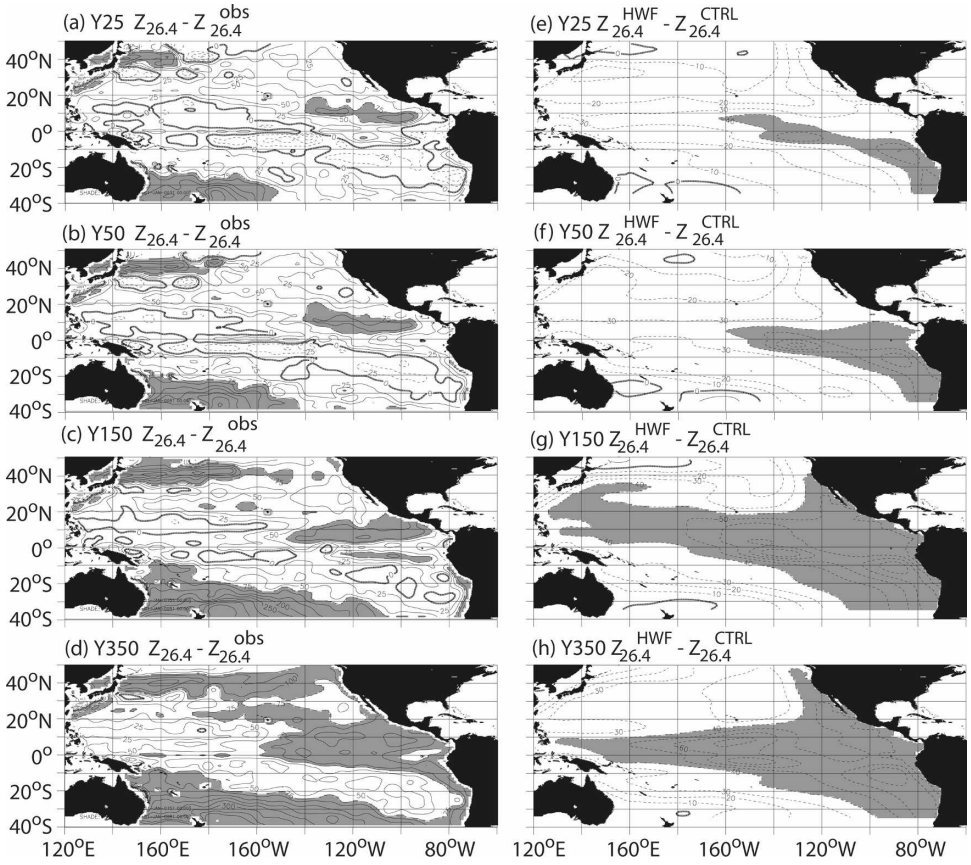

FIG. 11. (left) Cpld-HWF minus *WOA01* $z_{26.4}$ (contour interval = 25 m). Positive biases exceeding 75 m are shaded. (right) Cpld-HWF minus Cpld-CTRL $z_{26.4}$ (contour interval = 10 m). Negative values larger than 40 m are shaded.

America, near-surface temperature and salinity are moderately colder and fresher, respectively (not shown). Surface temperature and salinity are strongly damped by the air–sea fluxes. Zonal mean SST is ~0.2°C warmer and the zonal mean heat flux change is about -12 W m^{-2} at the equator. Off the equator, surface temperatures are less the 0.1°C cooler with a +1–3 W m^{-2} zonal average response. The heat flux sensitivity in the tropics is almost entirely due to changes in evaporative cooling. Precipitation is prescribed, so there is no change. Evaporation near the equator increases by ~0.25 mm day^{-1} and decreases off the equator by ~0.1 mm day^{-1} near 10° latitude. Heat flux into the Niño-3 region is reduced by ~12 W m^{-2} with a peak reduction of 20 W m^{-2} near 0°N, 120°W. Evaporation increases in the eastern equatorial upwelling region because of warmer entrainment temperatures. Heat uptake near the eastern boundary increases moderately, for example, ~4 W m^{-2} averaged in the Niño-1 + Niño-2 region (10°–0°S, 80°–90°W) with a peak increase of ~14 W m^{-2}. This is attributable to the presence of cooler entrainment temperatures below the mixed layer. Subsurface temperatures to depths of 350 m are 1°–2°C colder in the tropics. Cooling is concentrated near the base of the EUC at the equator, below the ITCZ, and along the eastern boundaries (Fig. 12). The along-isopycnal oceanic circulation is relatively unchanged and the entrainment from below $\sigma_\theta = 26.4$ is reduced by approximately 0.5–1 Sv, accounting for the negative basin-averaged trend in $z_{26.4}$ relative to UnCpld-CTRL. This compensates for about 20% of the positive trend in $z_{26.4}$ in the UnCpld-CTRL experiment.

b. *Cpld-HWF*

Figure 11 shows the difference in $z_{26.4}$ between Cpld-HWF and Cpld-CTRL. The response pattern is similar to the UnCpld experiments. Large-scale differences near year 350 are between 50 and 60 m in the eastern tropics. The $\sigma_\theta = 26.4$ surface is elevated from the eastern boundary to the midlatitudes. The $z_{26.4}$ bias in the Cpld-HWF run is approximately 30% less than that in

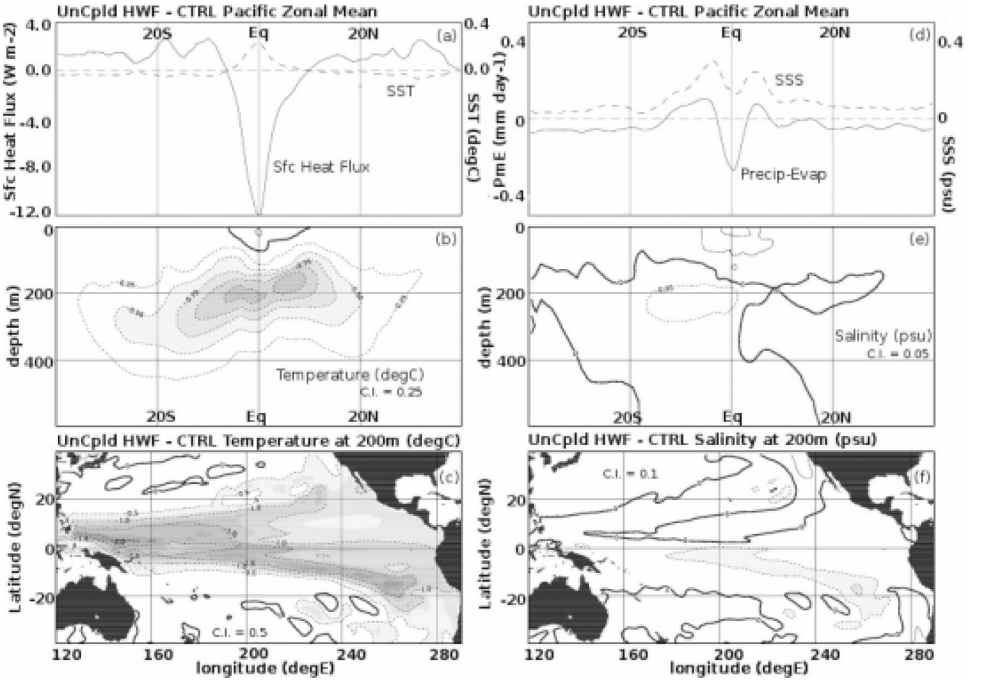

FIG. 12. UnCpld-HWF minus UnCpld-CTRL Pacific (a) zonal average heat flux difference (W m^{-2}; solid) and SST difference (°C; dashed); (b) zonal average temperature difference (contour interval = 0.25°C); (c) 200-m temperature difference (contour interval = 0.5°C); (d) zonal average PmE difference (mm day^{-1}; solid) and SSS difference (PSU; dashed); (e) zonal average salinity difference (contour interval = 0.05 PSU); and (f) 200-m salinity difference (contour interval = 0.1 PSU).

the Cpld-CTRL integration between years 100 and 400. Offshore of the U.S. West Coast, mean SST is ~1°C cooler. Peruvian near-coastal temperatures are ~0.5°C cooler. Zonal mean SST is slightly warmer at the equator and cooler off the equator (Fig. 13). Peak off-equatorial zonal mean cooling is about −0.6°C near 10°S. Zonal average SSS are generally fresher by ~0.1–0.2 PSU north of the equator and less than 0.1 PSU saltier near 10°S. SSS sensitivity is strongest along the U.S. West Coast, with peak freshening greater than 0.7 PSU near the California coast. The increase in zonal mean SSS near 10°S is mainly due to increased salinity in the western Pacific associated with a northward shift in the SPCZ. Zonal mean atmospheric heat flux decreases by ~8 W m^{-2} near the equator. The reduction in tropical ocean heat uptake is partitioned between an increase in evaporation and a reduction in incident shortwave due to an increase in cloudiness. Net precipitation in the tropics increases with a peak zonal mean increase of 0.8 mm day^{-1}. There is a zonal mean increase in evaporation off-equator near 10° latitude on either side of the equator. Niño-3 ocean heat uptake decreases by 10 W m^{-2} (12 W m^{-2} in UnCpld-HWF). Niño-1 + Niño-2 heat flux increases by approximately 5 W m^{-2}, similar to the 4 W m^{-2} change in the UnCpld-HWF experiment. Niño-3 SST variability is not impacted significantly. Niño-1 + Niño-2 interannual SST variability increases by ~10%. Subsurface temperatures are 2°–3°C cooler along the northern ITCZ and the eastern boundaries at 200 m. Subsurface salinities are generally fresher with peak change of ~ −0.5 PSU off the southern California coast.

Depth-integrated equatorward transport at 30°S increases by ~1 Sv between years 200 and 400 (Fig. 14), nearly all of which is at densities lighter than $\sigma_\theta = 26.4$. Equatorward transport at 30°N increases by ~0.5 Sv above $\sigma_\theta = 26.4$, with a compensating poleward return flow of 0.5 Sv below. ITF export increases by 0.5–1 Sv below $\sigma_\theta = 26.4$. The entrainment of intermediate waters decreases by 1–2 Sv, mainly in the western tropics. This circulation is balanced mainly by UL inflow from the Southern Ocean and LL outflow below $\sigma_\theta = 26.4$ through the ITF. The net imbalance between along-isopycnal divergence of UL water and entrainment of intermediate water is reduced by ~30% over the course of the run.

Averaged over the 400-yr model run and over the Pacific basin from 30°S to 30°N, oceanic heat export from the Pacific reduces by ~0.06 PW, largely due to a 0.07-PW increase in heat transport from the Southern

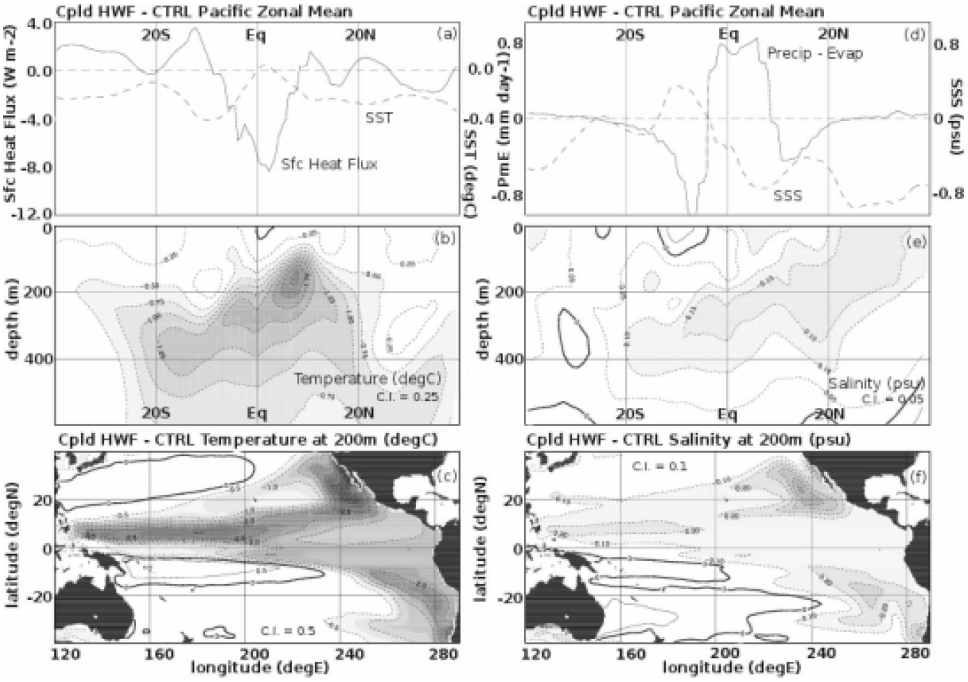

FIG. 13. Cpld-HWF minus Cpld-CTRL Pacific (a) zonal average heat flux difference (W m^{-2}; solid) and SST difference (°C; dashed); (b) zonal average temperature difference (contour interval = 0.25°C); (c) 200-m temperature difference (contour interval = 0.5°C); (d) zonal average PmE difference (mm day^{-1}; solid) and SSS difference (PSU; dashed); (e) zonal average salinity difference (contour interval = 0.05 PSU); and (f) 200-m salinity difference (contour interval = 0.1 PSU).

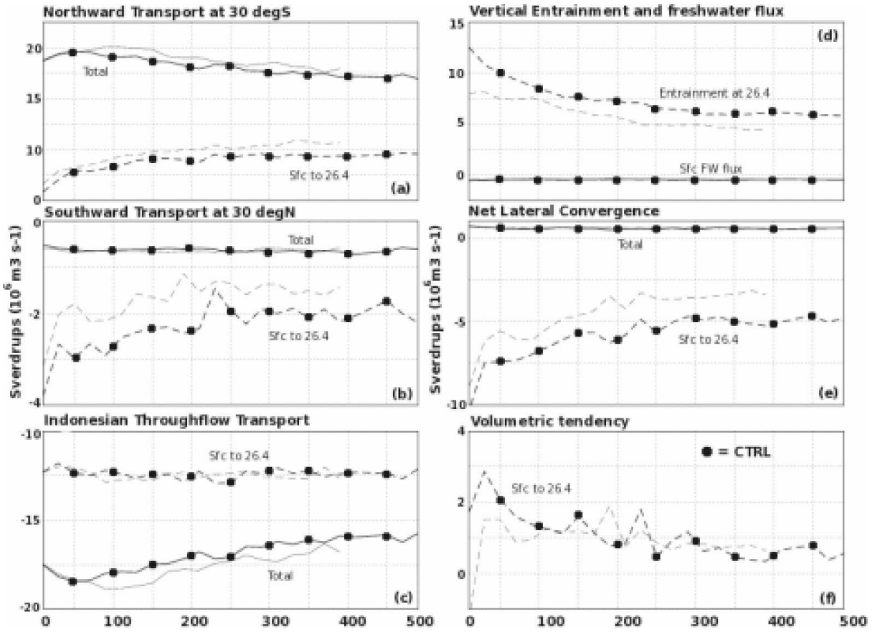

FIG. 14. Volumetric transports (Sv) within the Pacific basin from 30°S to 30°N. Cpld-CTRL (dotted lines) and Cpld-HWF (solid lines). Depth-integrated transports are solid and transports from the surface to $\sigma_\theta = 26.4$ are dashed. Positive values are in the basin: (a) 30°S, (b) 30°N; (c) Indonesian Throughflow; (d) net PmE from atmosphere (solid) and entrainment from below $\sigma_\theta = 26.4$ (dashed); (e) total lateral advection, and (f) $z_{26.4}$ tendency.

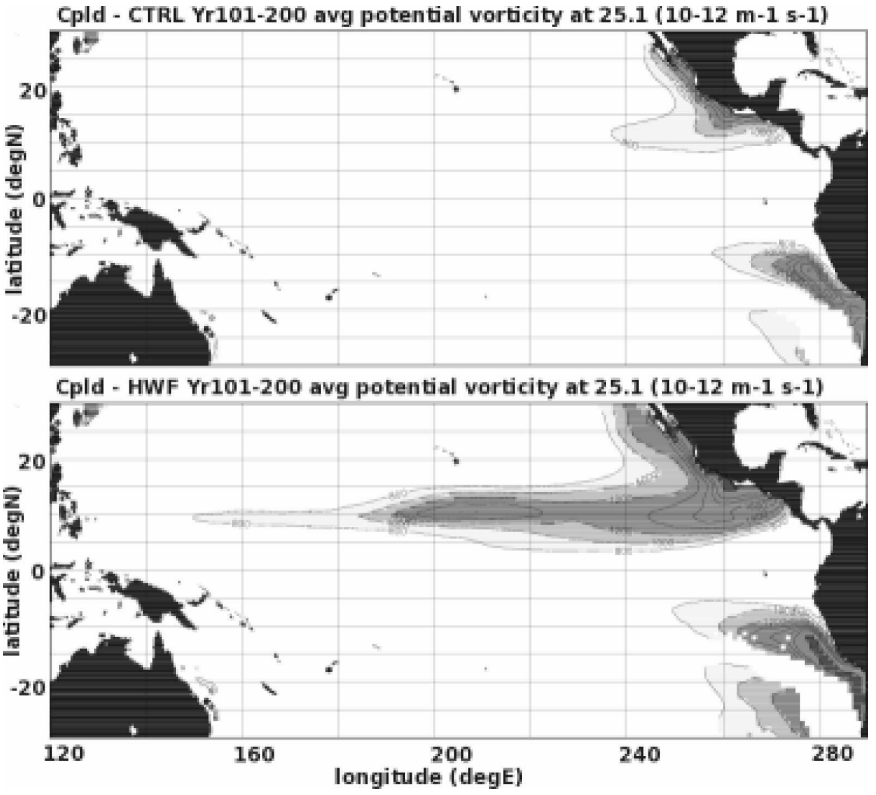

FIG. 15. Planetary potential vorticity at $\sigma_\theta = 25.1$ averaged between years 101–200 of (top) Cpld-CTRL and (bottom) Cpld-HWF. Based on monthly averages. Locations where the isopycnal layer does not exist or is contained within the mixed layer (based on 0.1 g kg^{-1} difference criteria from the surface) at least 1 month yr^{-1} are not shaded.

Ocean. Average ocean heat uptake from the atmosphere decreases by 0.09 PW. There is, therefore, a net ocean cooling impact from the HWF parameterization.

Figure 15 show the difference in Q at $\sigma_\theta = 25.1$ between years 101 and 200 of Cpld-CTRL and Cpld-HWF. This demonstrates the ability of the HWF diffusivity profile to increase stratification within the tropics, and along the northern ITCZ and the eastern coastal boundaries. This is relevant, for example, to advective pathways between the northern subtropics and the equator. Elevated stratification along the eastern boundaries can impact entrainment temperatures in important upwelling regions offshore of the United States and the Peruvian coast as well.

c. *Cpld-LOW*

An additional experiment with a uniform upper-ocean diffusivity of 10^{-6} m^2 s^{-1} was integrated for 150 yr in the Cpld configuration (Fig. 16). During years 0–50 of this run, $z_{26.4}$ tropical biases are reversed. The tropical pycnocline is more than 50 m shallower than the observations, except near the Costa Rica Dome where the errors are similar to the UnCpld-CTRL experiment. On longer time scales, the $z_{26.4}$ reduction in the tropics is opposed by an increase in the midlatitudes. Positive biases are larger than UnCpld-CTRL in the subtropics. Lower diffusivities in high latitudes further reduce the already anemic mid- and high-latitude intermediate water production found in the Cpld-CTRL experiment. This leads to an accumulation of fluid at densities less than $\sigma_\theta = 26.4$ and a shift in the form of light mode waters and a deepening of the interior pycnocline in this region. These errors subsequently propagate into the subtropics. Basin-averaged $z_{26.4}$ bias exceeds Cpld-CTRL after 150 yr with a monotonic trend relative to Cpld-CTRL after year 50. Overall, the extratropical patterns are consistent with a general sharpening of the pycnocline—the $\sigma_\theta = 26.4$ surface moves upward relative to the control integration where it is deep, and downward where it is shallow. The contrast with the uniform upward displacement emanating from tropics in Cpld-HWF is quite striking.

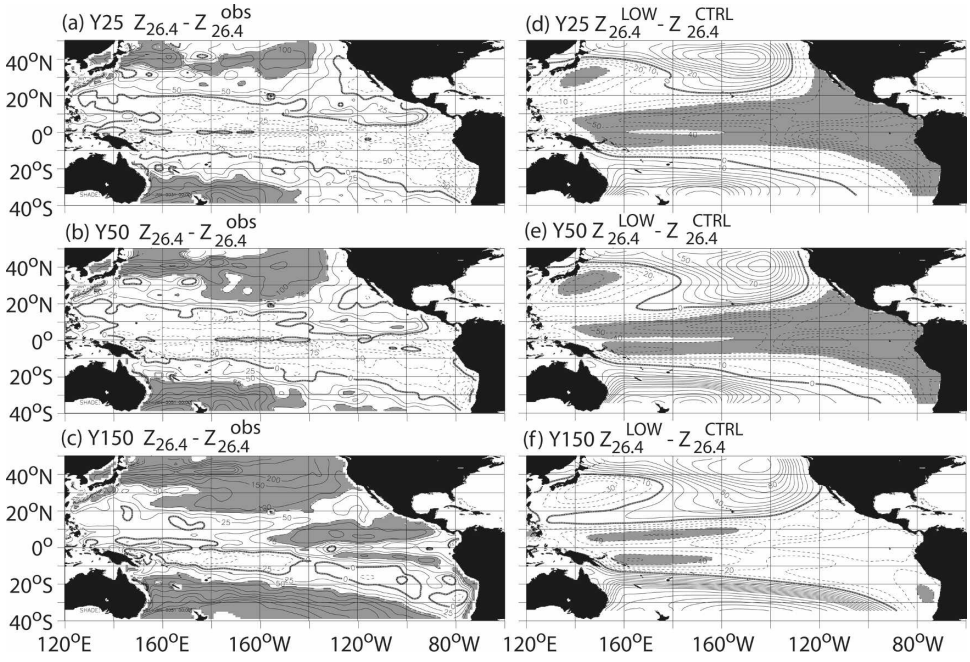

FIG. 16. (left) Cpld-Low minus *WOA01* $z_{26.4}$ (contour interval = 25 m). Positive biases exceeding 75 m are shaded. (right) Cpld-Low minus Cpld-CTRL $z_{26.4}$ (contour interval = 10 m). Negative values larger than 40 m are shaded.

Along-isopycnal UL transport convergence from the midlatitudes increases by 6–8 Sv and UL ITF transport into the Indian Ocean decreases by ~1 Sv. Entrainment from below $\sigma_\theta = 26.4$ decreases by ~6–7 Sv. The net imbalance increases by ~1–2 Sv in the 200-yr coupled run, thereby depressing the $\sigma_\theta = 26.4$ surface on average. It is clear from this experiment that a uniform reduction in diffusivity reduces midlatitude and subpolar dense water production and acts to warm the subsurface in the midlatitudes while cooling the subsurface in the tropics, as in the HWF experiments.

5. Summary and discussion

An isopycnal ocean model sensitivity to a gravity wave dissipation parameterization with a pronounced equatorial drop-off is evaluated by coupling both to a fixed atmospheric boundary layer and in a global general circulation model. The reduction in entrainment of intermediate waters (denser than $\sigma_\theta = 26.4$) in the western tropics increases the stratification in the pycnocline and cools the upper tropical Pacific. This perturbation is effectively redistributed along the eastern boundary by Kelvin and coastally trapped waves. The depth of the $\sigma_\theta = 26.4$ surface is elevated by as much as 60 m near the eastern boundary and in the eastern tropics in a 400-yr coupled experiment. Estimated bias reduction averaged over the Pacific basin is approximately 30%. Compensating inflow from the Southern Ocean at densities lighter than $\sigma_\theta = 26.4$ and outflow through the ITF at densities greater than $\sigma_\theta = 26.4$ occurs in the coupled model.

In the UnCpld experiment, ocean evaporative heat loss increases in the eastern equatorial Pacific. The reduction in the downward diffusion of heat across the ocean thermocline is balanced by increased evaporation due to the presence of warmer entrainment temperatures below the mixed layer. In the Cpld run, an increase in tropical cloudiness, in addition to increased evaporation, combine to produce a similar reduction in atmospheric heat update. Zonal mean temperatures are 1°–2°C cooler between 100 and 350 m in the tropics. Cooling extends along the eastern boundary, mimicking the adjustment in $z_{26.4}$, with peak temperature decrease of 1°–2°C between 50 and 100 m along the subtropical eastern boundary. In the Cpld run, oceanic heat transport from the Pacific decreases by ~0.06 PW, mainly due to a 0.07-PW increase in the equatorward transport from the Southern Ocean. Heat uptake from the atmosphere reduces by 0.09 PW.

Lowering the diapycnal diffusivity everywhere to a constant value of 10^{-6} m^2 s^{-1} increases midlatitude biases substantially. The increase in the along-isopycnal flux of water at densities less than $\sigma_\theta = 26.4$ into the

Pacific exceeds the reduction in diffusive entrainment of intermediate water masses from below $\sigma_\theta = 26.4$ in this experiment. This results in a larger $z_{26.4}$ bias relative to the control experiment. The HWF parameterization, with low equatorial diffusivity and midlatitude diffusivities relatively unchanged, produces the best fit to observations.

This result highlights the importance of investigating spatial variations in background diffusivity as contributing factors to the maintenance of the vertical structure of the pycnocline. These results also indicate that it is important to use ocean models that are capable of exhibiting extremely small (less than 10^{-6} m^2 s^{-1}) numerical diapycnal diffusivities if the full effects of ocean turbulence on climate are to be realized.

Acknowledgments. The authors thank Anand Gnanadesikan, Stephen Griffies, and Kirk Bryan for reviewing early versions of this manuscript. Special thanks to Geoffrey Vallis for several valuable discussions. We also thank the GFDL model development teams for their hard work in developing the model software framework that made this study possible. Cathy Raphael and Jeff Varanyak are acknowledged for their figure preparation. Data visualization and analysis was performed almost exclusively with Ferret (http://ferret.pmel.noaa.gov); Argo figures were generated using Ocean Data View (http://odv.awi.de).

REFERENCES

Alford, M. H., 2003: Redistribution of energy available for ocean mixing by long-range propagation of internal waves. *Nature,* **423,** 159–162.

Anderson, W. G., A. Gnanadesikan, R. Hallberg, J. Dunne, and B. L. Samuels, 2007: Impact of ocean color on the maintenance of the Pacific cold tongue. *Geophys. Res. Lett.,* **34,** L11609, doi:10.1029/2007GL030100.

Bingham, F. M., 1992: Formation and spreading of subtropical mode water in the North Pacific. *J. Geophys. Res.,* **97,** 11 177–11 189.

Bryan, F., 1987: Parameter sensitivity of primitive equation ocean general circulation models. *J. Phys. Oceanogr.,* **17,** 970–985.

Bryan, K., and L. J. Lewis, 1979: A water mass model of the world ocean. *J. Geophys. Res.,* **84,** 2503–2517.

Canuto, V. M., A. Howard, Y. Cheng, and R. L. Miller, 2004: Latitude-dependent vertical mixing and the tropical thermocline in a global OGCM. *Geophys. Res. Lett.,* **31,** L16305, doi:10.1029/2004GL019891.

Conkright, M. E., and Coauthors, 2002: *Introduction.* Vol. 1, *World Ocean Atlas 2001,* NOAA Atlas NESDIS 42, 160 pp.

Dai, A., 2006: Precipitation characteristics in eighteen coupled climate models. *J. Climate,* **19,** 4605–4630.

Delworth, T. L., and Coauthors, 2006: GFDL's CM2 global coupled climate models. Part I: Formulation and simulation characteristics. *J. Climate,* **19,** 643–674.

Endoh, T., and T. Hibiya, 2006: Numerical study of the meridional overturning circulation with mixing hotspots in the Pacific Ocean. *J. Oceanogr.,* **62,** 259–266.

Fine, R. A., R. Lukas, F. M. Bingham, M. J. Warner, and R. H. Gammon, 1994: The western equatorial Pacific: A water mass crossroads. *J. Geophys. Res.,* **99,** 25 063–25 080.

Garrett, C. J. R., and W. H. Munk, 1991: Space-time scales of internal waves: A progress report. *J. Geophys. Res.,* **80,** 291–297.

Gent, P., and J. C. McWilliams, 1990: Isopycnal mixing in ocean circulation models. *J. Phys. Oceanogr.,* **20,** 150–155.

GFDL Atmospheric Model Development Team, 2004: The new GFDL global atmosphere and land model AM2–LM2: Evaluation with prescribed SST simulations. *J. Climate,* **17,** 4641–4673.

Gnanadesikan, A., R. D. Slater, and B. L. Samuels, 2003: Sensitivity of water mass transformation and heat transport to subgridscale mixing in coarse-resolution ocean models. *Geophys. Res. Lett.,* **30,** 1967, doi:10.1029/2003GL018036.

Gregg, M. C., T. B. Sanford, and D. P. Winkel, 2003: Reduced mixing from the breaking of internal waves in equatorial waters. *Nature,* **422,** 477–478.

Griffies, S. M., R. C. Pacanowski, and R. W. Hallberg, 2000: Spurious diapycnal mixing associated with advection in a *z*-coordinate ocean model. *Mon. Wea. Rev.,* **128,** 538–564.

——, and Coauthors, 2005: Formulation of an ocean model for global climate simulations. *Ocean Sci.,* **1,** 45–79.

Hallberg, R., 2000: Time integration of diapycnal diffusion and Richardson number–dependent mixing in isopycnal coordinate ocean models. *Mon. Wea. Rev.,* **128,** 1402–1419.

——, 2003: The suitability of large-scale ocean models for adapting parameterizations of boundary mixing and a description of a refined bulk mixed layer model. *Near-Boundary Processes and Their Parameterization: Proc. 'Aha Huliko'a Hawaiian Winter Workshop,* Honolulu, HI, University of Hawaii at Manoa, 187–203.

——, and A. Gnanadesikan, 2006: The role of eddies in determining the structure and response of the wind-driven Southern Hemisphere overturning: Results from the Modeling Eddies in the Southern Ocean (MESO) project. *J. Phys. Oceanogr.,* **36,** 2232–2252.

Hayes, S., L. Magnum, J. Picaut, A. Sumi, and K. Takeuchi, 1991: A moored array for real-time measurements in the tropical Pacific Ocean. *Bull. Amer. Meteor. Soc.,* **72,** 339–347.

Henyey, F. S., J. Wright, and S. M. Flatté, 1986: Energy and action flow through the internal wave field: An eikonal approach. *J. Geophys. Res.,* **91,** 8487–8496.

Jackson, L., R. Hallberg, and S. Legg, 2008: A parameterization of shear-driven turbulence for ocean climate models. *J. Phys. Oceanogr.,* **38,** 1033–1053.

Johnson, G. C., and D. W. Moore, 1997: The Pacific subsurface countercurrents and an inertial model. *J. Phys. Oceanogr.,* **27,** 2448–2459.

——, and M. J. McPhaden, 1999: Interior pycnocline flow from the subtropical to the equatorial Pacific Ocean. *J. Phys. Oceanogr.,* **29,** 3073–3089.

Jones, J., 1973: Vertical mixing in the equatorial undercurrent. *J. Phys. Oceanogr.,* **3,** 286–296.

Kessler, W. S., 2002: Mean three-dimensional circulation in the northeast tropical Pacific. *J. Phys. Oceanogr.,* **32,** 2457–2471.

Large, W., and S. Yeager, 2004: Diurnal to decadal global forcing for ocean and sea-ice models: The data sets and flux climatologies. NCAR Tech. Note NCAR/TN-460+STR, 105 pp.

Legg, S., and K. M. Huijts, 2006: Preliminary simulations of internal waves and mixing generated by finite amplitude tidal flow over isolated topography. *Deep-Sea Res.,* **53,** 140–156.

Lock, A. P., A. R. Brown, M. R. Bush, G. M. Martin, and R. N. Smith, 2000: A new boundary layer mixing scheme. Part I: Scheme description and single column model tests. *Mon. Wea. Rev.,* **128,** 3187–3199.

Lu, P., and J. P. McCreary, 1995: Influence of the ITCZ on the flow of thermocline water from the subtropical to the equatorial pacific ocean. *J. Phys. Oceanogr.,* **25,** 3076–3088.

Luyten, J. R., J. Pedlosky, and H. Stommel, 1983: The ventilated thermocline. *J. Phys. Oceanogr.,* **13,** 292–309.

McCreary, J. P., and P. Lu, 1994: Interaction between the subtropical and equatorial ocean circulations: The subtropical cell. *J. Phys. Oceanogr.,* **24,** 466–497.

——, ——, and Z. Yu, 2002: Dynamics of the Pacific subsurface countercurrents. *J. Phys. Oceanogr.,* **32,** 2379–2404.

Meehl, G. A., P. R. Gent, J. M. Arblaster, B. L. Otto-Bliesner, E. C. Brady, and A. Craig, 2001: Factors that affect the amplitude of El Niño in global coupled climate models. *Climate Dyn.,* **17,** 515–526.

Milliff, R. F., J. Morzel, D. B. Chelton, and M. H. Freilich, 2004: Wind stress curl and wind stress divergence biases from rain effects on QSCAT surface wind retrievals. *J. Atmos. Oceanic Technol.,* **21,** 1216–1231.

Moorthi, S., and M. J. Suarez, 1992: Relaxed Arakawa–Shubert: A parameterization of moist convection for general circulation models. *Mon. Wea. Rev.,* **120,** 978–1002.

Murray, R. J., 1996: Explicit generation of orthogonal grids for ocean models. *J. Comput. Phys.,* **126,** 251–273.

Pedlosky, J., 1983: Eastern boundary ventilation and the structure of the thermocline. *J. Phys. Oceanogr.,* **13,** 2038–2044.

Peters, H., M. C. Gregg, and T. B. Sanford, 1995: Detail and scaling of turbulent overturns in the Pacific equatorial undercurrent. *J. Geophys. Res.,* **100,** 18 349–18 368.

Roemmich, D., and B. Cornuelle, 1992: The subtropical mode waters of the South Pacific Ocean. *J. Phys. Oceanogr.,* **22,** 1178–1187.

Rowe, G., E. Firing, and G. Johnson, 2000: Pacific equatorial subsurface countercurrent velocity, transport, and potential vorticity. *J. Phys. Oceanogr.,* **30,** 1172–1187.

Samelson, R., and G. K. Vallis, 1997: Large-scale circulation with small diapycnal diffusion: The two-thermocline limit. *J. Mar. Res.,* **2,** 223–275.

Sarmiento, J. L., N. Gruber, M. A. Brzezinski, and J. P. Dunne, 2003: High latitude controls of thermocline nutrients and low latitude biological productivity. *Nature,* **427,** 56–60.

Simmons, H. L., S. R. Jayne, L. C. St. Laurent, and A. J. Weaver, 2004: Tidally driven mixing in a numerical model of the general circulation. *Ocean Modell.,* **6,** 245–263.

Suga, T., Y. Takei, and K. Hanawa, 1997: Thermostad distribution in the North Pacific subtropical gyre: The central mode water and the subtropical mode water. *J. Phys. Oceanogr.,* **27,** 140–152.

Talley, L., Y. Nagata, M. Fujimura, T. Iwao, T. Kono, D. Inagake, M. Hirai, and K. Okuda, 1995: North Pacific intermediate water in the Kuroshio/Oyashio mixed water region. *J. Phys. Oceanogr.,* **25,** 475–501.

Toggweiler, J. R., K. Dixon, and W. S. Broecker, 1991: The Peru upwelling and the ventilation of the South Pacific thermocline. *J. Geophys. Res.,* **96,** 20 467–20 497.

Tsuchiya, M., 1981: The origin of the Pacific equatorial 13°C water. *J. Phys. Oceanogr.,* **11,** 794–812.

Vallis, G. K., 2000: Large-scale circulation and production of stratification: Effects of wind, geometry, and diffusion. *J. Phys. Oceanogr.,* **30,** 933–954.

Winton, M., 2000: A reformulated three-layer sea ice model. *J. Atmos. Oceanic Technol.,* **17,** 525–531.

Wittenberg, A. T., A. Rosati, N. C. Lau, and J. J. Ploshay, 2006: GFDL's CM2 global coupled climate models. Part III: Tropical Pacific climate and ENSO. *J. Climate,* **19,** 698–722.

Wong, A. P., and G. C. Johnson, 2003: South Pacific eastern subtropical mode water. *J. Phys. Oceanogr.,* **33,** 1493–1509.

Wright, D. G., 1997: An equation of state for use in ocean models: Eckart's formula revisited. *J. Atmos. Oceanic Technol.,* **14,** 735–740.

Xie, S. P., H. Xu, W. S. Kessler, and M. Nonaka, 2005: Air–sea interaction over the eastern Pacific warm pool: Gap winds, thermocline dome, and atmospheric convection. *J. Climate,* **18,** 5–20.

Yu, Z., and P. S. Schopf, 1997: Vertical eddy mixing in the tropical upper ocean: Its influence on zonal currents. *J. Phys. Oceanogr.,* **27,** 1447–1458.